Atomic Structure and Dynamics of Epitaxial Platinum Bilayers on Graphene

Alex W. Robertson,[1] Gun-Do Lee,[2,3]* Sungwoo Lee,[2,3] Parker Buntin,[4] Matthew Drexler,[4] Ali Abdelhafiz,[4] Euijoon Yoon,[2,3] Jamie H. Warner,[1] Faisal M. Alamgir[4]**

[1] Department of Materials, University of Oxford, Parks Road, Oxford, OX1 3PH, United Kingdom

[2] Department of Materials Science and Engineering, Seoul National University, Gwanak-gu, Seoul 08826, South Korea

[3] Research Institute of Advanced Materials, Seoul National University, Gwanak-gu, Seoul 08826, Republic of Korea

[4] School of Materials Science and Engineering, Georgia Institute of Technology, Atlanta, GA 30332, USA

*alex.w.robertson@gmail.com; gdlee@snu.ac.kr; faisal.alamgir@mse.gatech.edu

Abstract Platinum atomic layers grown on graphene were investigated by atomic resolution transmission electron microscopy (TEM). These TEM images reveal the epitaxial relationship between the atomically thin platinum layers and graphene, with two optimal epitaxies observed. The energetics of these epitaxies influences the grain structure of the platinum film, facilitating grain growth *via* in-plane rotation and assimilation of neighbor grains, rather than grain coarsening from the movement of grain boundaries. This

growth process was enabled due to the availability of several possible low energy intermediate states for the rotating grains; the Pt-Gr epitaxies, which are minima in surface energy; and coincident site lattice grain boundaries, which are minima in grain boundary energy. Density functional theory (DFT) calculations reveal a complex interplay of considerations for minimizing the platinum grain energy, with free platinum edges also having an effect on the relative energetics. We thus find that the platinum atomic layer grains undergo significant reorientation to minimize interface energy (*via* epitaxy), grain boundary energy (*via* low-energy orientations), and free edge energy. These results will be important for the design of two-dimensional graphene supported platinum catalysts and obtaining large-area uniform platinum atomic layer films, and also provide fundamental experimental insight in to the growth of heteroepitaxial thin-films.

Keywords: Platinum, catalyst, graphene, monolayer, TEM, heteroepitaxial thin-film, grain growth

Despite its expense, platinum remains an indispensable catalysts. Its catalytic activity is essential for many reactions in the chemical industry,[1] and nanostructured platinum is currently one of the most effective catalysts for facilitating the slow oxygen reduction reaction (ORR) of proton electrolyte membrane fuel cells (PEMFCs),[2–5] and the generation of hydrogen by the hydrogen evolution reaction (HER).[6,7] The price of platinum is a fundamental barrier to the scale-up of applications that depend on platinum catalyzed reactions. Finding replacements that do not consist of platinum-group metals is a large and active area of research, spanning through doped two-dimensional materials to cheaper transition metals.[8–13] An alternative approach is to maintain the effective surface area while reducing the mass-loading of platinum, such as by preparing compound nanoparticles or by arranging as single atoms.[14–20]

One strategy is to form platinum atomic layers on a host material, such as by preparing a platinum-shell core-shell nanoparticle, with single atom thick platinum layers possible by performing galvanic

replacement of a sacrificial copper layer.[21–24] Potentially more desirable would be to synthesize a platinum atomic layer across the surface of a planar substrate, as this would avoid some of the degradation issues that afflict metal nanoparticles, such as Ostwald ripening and support detachment.[25–27] However growth of atomic level films has proven challenging, often requiring the precious metal gold. These include platinum monolayer films on palladium and gold (111) surfaces,[28,29] monolayer deposition on a gold coated nickel foam,[30] and an assembly of nano-islands of platinum on gold and silicon.[31] Without needing another noble metal, promising results have been obtained by thermal evaporation of platinum to a tungsten carbide substrate, with Pt {111} orientation depositing on the WC {001} face, yielding monolayers of platinum on the WC.[32] Recently we showed that graphene can be used as an aid to templated growth of platinum monolayers on gold,[33] yielding a shielded platinum catalyst suitable for the harsh low-pH environment of a PEMFC cathode.[34] Unlike for previous reports of platinum and graphene epitaxy,[35] where graphene monolayers were deposited on bulk platinum, we found that the platinum monolayers oriented with the [001] axis orthogonal to the growth plane, rather than matching along a {111} face.

Here we present an in-depth investigation at the atomic structure and dynamics of the platinum atomic layers, and their interaction with the graphene substrate. Other metallic monolayers on graphene have been reported, including gold and iron,[36–39] however the potential importance of the graphene-platinum hybrid as a catalyst system makes a detailed investigation of its atomic structure and stability desirable. By combining atomic resolution TEM imaging with density functional theory (DFT) calculations, we show that there are two primary epitaxial configurations that are stable. The edge of the platinum layers play an influential role in the energetic favorability of grain orientation, as does the minimization of grain boundary energy *via* formation of coincident site lattice (CSL) satisfying grain boundaries. These

energetics were found to strongly influence grain growth, which was driven by rotation and assimilation rather than by the standard mechanism of grain boundary curvature minimization.[40,41]

Results and Discussion

Platinum was grown on graphene as detailed in prior work.[33] Aberration corrected (AC-) TEM imaging of the sample revealed areas decorated with thin crystals of platinum, along with some areas of bulk platinum (Figure S1 and S2). The regions of thin platinum were found to exhibit a four-coordinate planar tetragonal crystal structure in the monolayer,[42] or a simple cubic in few-layers, as opposed to face-centered cubic of bulk platinum (Figure S1 and S3). We did not find evidence of the platinum layers undergoing out-of-plane buckling to lower energy, as found for free-space calculations,[42] likely due to the interaction with the graphene support. By performing box averaged intensity line profiles it was possible to determine that the platinum films were predominantly bilayer, with occasional monolayer areas also found (Figure S3).

The platinum atomic layers exhibited two modes of epitaxy with the graphene substrate. Figure 1 shows two instances of a platinum bilayer on graphene. In the first configuration the platinum atomic rows, the Pt {100} planes, are oriented parallel to the graphene zigzag axis (Figure 1a-d). In the second arrangement, the platinum bilayer is oriented such that the Pt {110} are parallel to a graphene zig-zag axis (Figure 1e-h). Magnified real space images (Figures 1b and f) have been annotated to show the lattice structures, and lines indicating the matching crystallographic planes. Fast Fourier transforms (FFTs) extracted from the AC-TEM images (Figure 1c and g, and Figure S4) reveal the epitaxy, with annotations for the hexagonal graphene and square platinum reflections showing the two different orientations. Atomic models of these two configurations, Figures 1d and h, illustrate the parallel directions with an arrow along the appropriate Pt {100} and Pt {110}, respectively. We will refer to these two modes of epitaxy as $Pt_{100}Gr_{zz}$ and $Pt_{110}Gr_{zz}$, indicating which platinum plane is parallel to the graphene zigzag for epitaxy, in the rest of the manuscript.

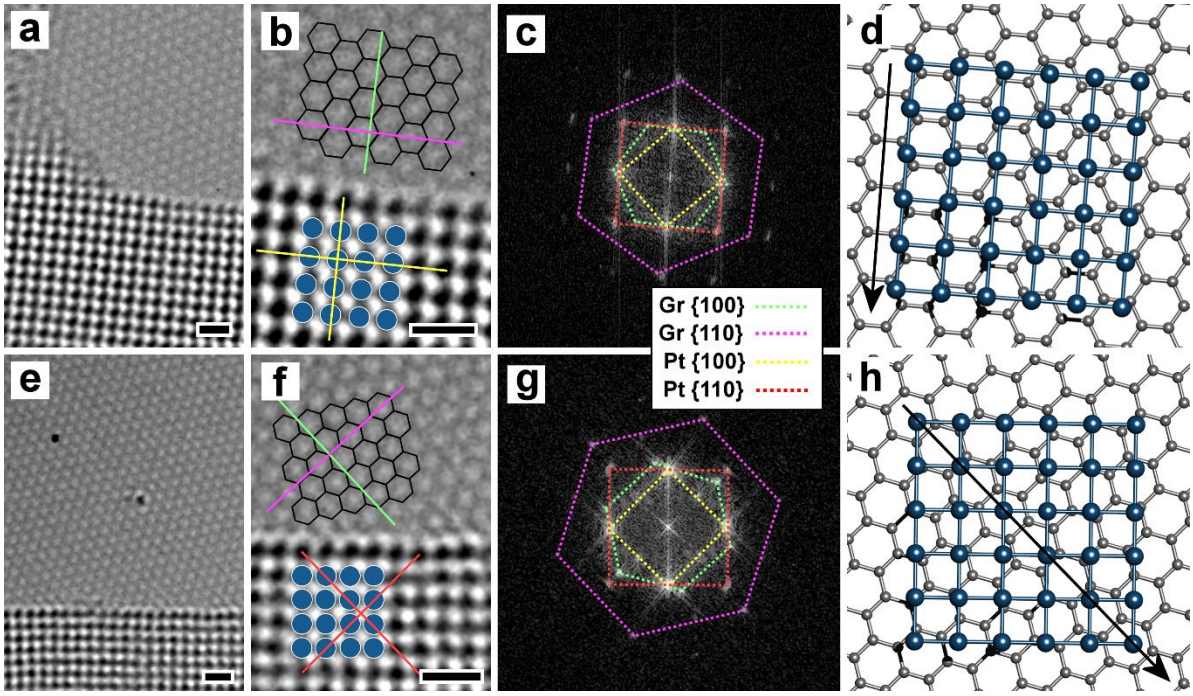


Figure 1. Epitaxial modes of Pt bilayers on graphene. (a) AC-TEM image of bilayer Pt, showing alignment between the Pt {100} and graphene zigzag. (b) Annotated magnified view of (a), showing the relative alignment of the Pt atomic sites to the graphene lattice. (c) FFT from (a), with annotations denoting the Pt and graphene orientations. (d) Atomic model representation of a-c, with an arrow indicating the Pt {100} axis parallel to a graphene zigzag ($Pt_{100}Gr_{zz}$). (e) AC-TEM image of bilayer Pt, showing alignment between the Pt {110} and graphene zigzag. (f) Annotated magnified view of (e), showing the relative alignment of the Pt atomic sites to the graphene lattice. (g) FFT from (f), with annotations denoting the Pt and graphene orientations. (h) Atomic model representation of e-g, with an arrow indicating the Pt {110} axis parallel to a graphene zigzag ($Pt_{110}Gr_{zz}$). Scale bars are 0.5 nm in all cases. Comparative image simulations are shown in Supporting Figure S5.

For comparison, in Figure 2a-d we show an AC-TEM time series demonstrating the epitaxial reconfigurations of a small, thin platinum crystal on the graphene surface, in contrast to the larger film of Figure 1. Corresponding FFTs (Figure 2e-h) reveal the epitaxial matching between platinum and graphene. In Figure 2a the platinum exhibits the same simple cubic structure as in Figure 1, with {100} lattice reflections at 0.23 nm, viewed down its [001] axis. The crystal is oriented with the Pt {100} along a

graphene zigzag ($Pt_{100}Gr_{zz}$), as in Figure 1a-d. In Figure 2b, the crystal has reconfigured into face-centered cubic stacking (FCC), likely due to sufficient Pt atoms accumulating in the out-of-plane direction, with the Pt {200} parallel to the graphene armchair axis. The FFT (Figure 2f) exhibits {200} reflections at 0.23 nm and {111} reflections at 0.27 nm, suggesting that the FCC reconfiguration maintains the non-bulk Pt lattice constant. The FCC crystal then rearranges to find a new epitaxial orientation (Figure 2c), now with the Pt {200} parallel to a graphene zigzag. Finally we observed the crystal revert back to a simple cubic structure, with the Pt {110} parallel to the graphene zigzag. This image sequence was acquired over 2m 45s.

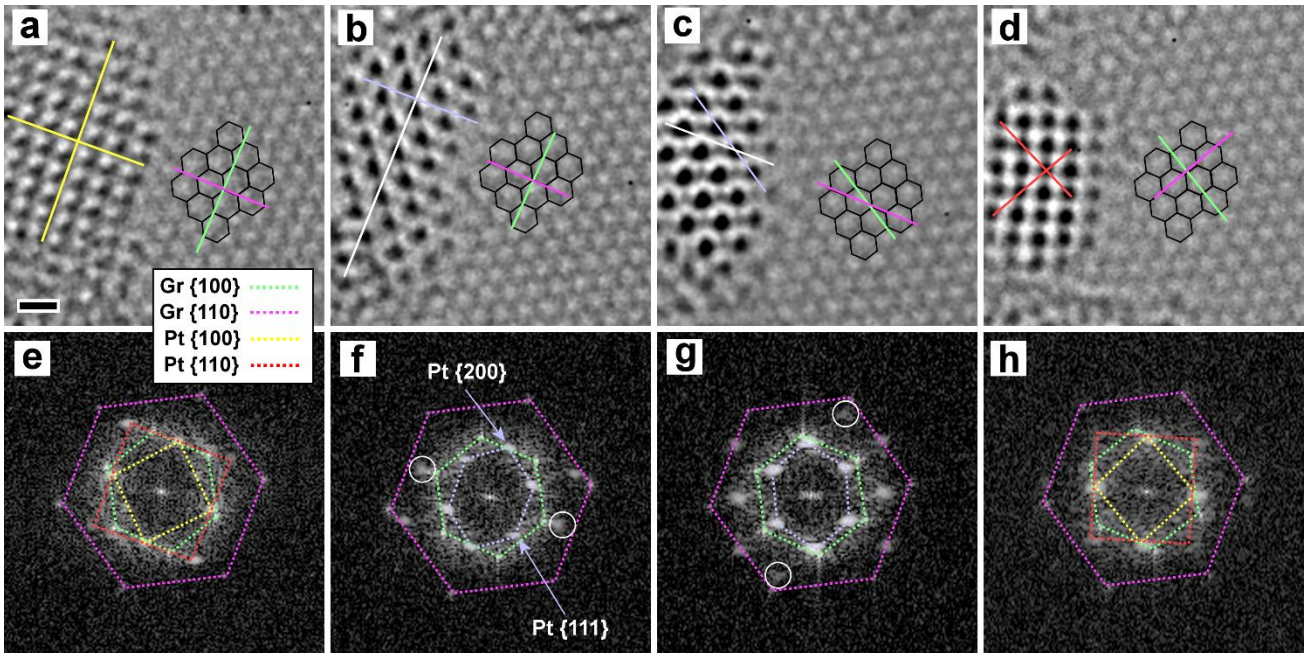


Figure 2. Epitaxial evolution of a small Pt crystal. (a-d) Time series of AC-TEM images and (e-h) corresponding FFTs, showing a Pt crystal reconfiguring through various epitaxial configurations with the graphene. In (b) and (c) the Pt is being viewed down a [110] axis with FCC stacking. Scale bar 0.5 nm.

The rapid changes between the two different epitaxies observed in Figure 2 (and in Figure S6) indicate that the two modes have similar relative energetics. The electron beam is able to provide sufficient energy for these small crystals to reconfigure between the two minima, acting analogously to a high temperature

annealing environment. The 15° rotation required to move between the two epitaxies is relatively small, allowing for the Pt bilayers to undergo atomic reconstruction under the electron beam in order to find the energetically most favorable alignment. To investigate this further density functional theory (DFT) calculations of our Pt bilayer/graphene system were performed. The DFT optimized structures of $Pt_{110}Gr_{zz}$ and $Pt_{100}Gr_{zz}$ are shown in Supporting Figure S7. After determining the optimal Pt-graphene distance, and confirming there was no significant difference for this between the two epitaxies (Figure 3a), we calculated the relative energetics for a platinum bilayer at a range of rotations on the graphene (Figure 3b). These revealed that the experimentally observed epitaxies are minima in the energy plot, with a small 30 meV difference in preference in favor of the $Pt_{110}Gr_{zz}$ epitaxial mode. The DFT analysis of partial density of states confirms the physisorption by van der Waals interaction between graphene layer and Pt layer because there is no evidence of orbital overlap. However, the charge density plot (Supporting Figure S8) shows the slight shift of electrons from graphene to Pt in common for $Pt_{110}Gr_{zz}$ and $Pt_{100}Gr_{zz}$.

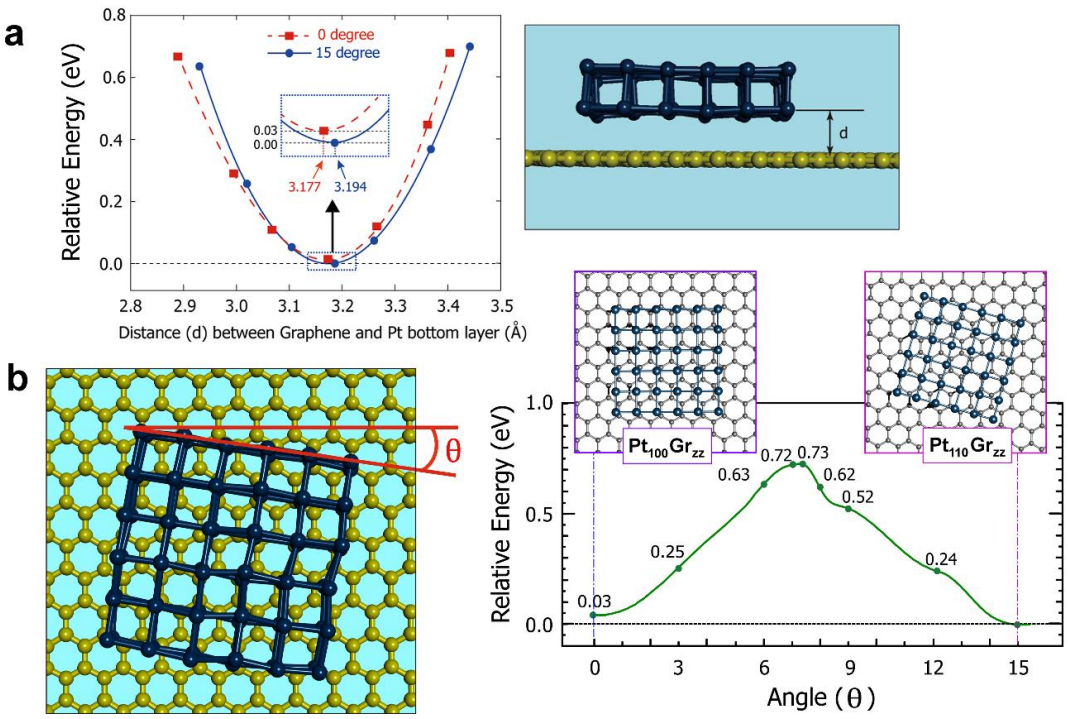


Figure 3. Energetics of the Pt bilayer epitaxial relationship with graphene. (a) DFT modeled energy diagram showing the optimal inter-layer distance between the platinum and graphene. Red is for $Pt_{100}Gr_{zz}$ and blue for $Pt_{110}Gr_{zz}$. (b) Calculated relative energies for Pt bilayer on graphene for different rotational alignments.

We observed grain rotation and growth in the heteroepitaxial Pt thin film, with the electron beam providing the energy to anneal the film and promote secondary grain growth at the expense of neighboring grains. Figure 4 shows an AC-TEM time-series of grain growth by rotation and assimilation of two grains. The initial configuration (Figure 4a) shows three adjacent Pt grains, with the top and central grains both exhibiting $Pt_{100}Gr_{zz}$ epitaxy (30° rotation), and the bottom grain unaligned but nearest to a $Pt_{110}Gr_{zz}$ epitaxy. Over the course of several minutes of continued imaging (Figure 4b-e), we observed the bottom two grains both gradually rotate and eventually both fall into a $Pt_{110}Gr_{zz}$ epitaxy, forming a complete grain. Interestingly, the center (blue) grain, which already exhibited epitaxy, deviated from this energetically favorable epitaxial configuration, leaving the system in an intermediate state where neither the blue nor yellow grain exhibited any epitaxy (Figure 4c and d). The yellow grain was also able to enter an epitaxy

of its own quickly (Figure 4b), however still deviated from this during the rotational assimilation process. This gradual shallowing of the grain boundary by grain rotation is distinct from the traditional picture of grain growth of atom-by-atom transfer from grain boundary migration,[43] and has been modelled and experimentally observed as a prominent grain growth mechanism in nanocrystalline thin films.[44]

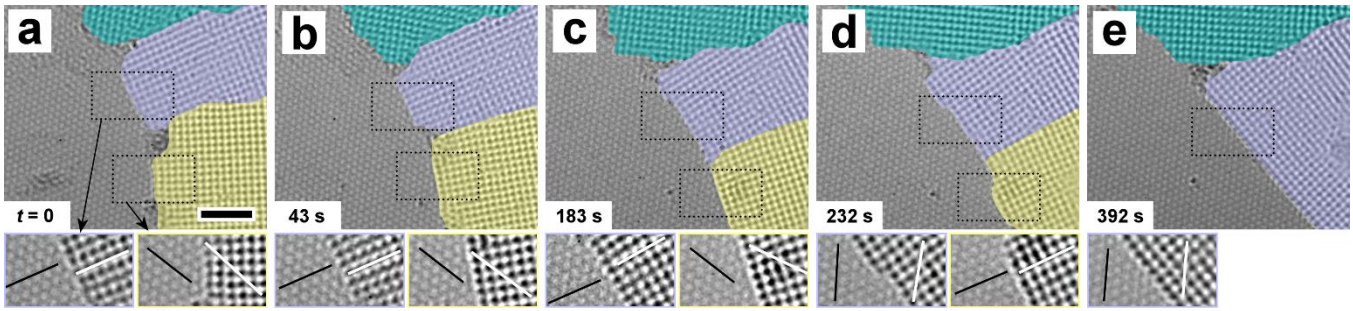


Figure 4. Pt grain rotation and assimilation. (a-e) AC-TEM image sequence of grain growth. (a) The blue (middle) grain is $Pt_{100}Gr_{zz}$, and the yellow (bottom) grain is ~5° from $Pt_{110}Gr_{zz}$. (b) The yellow ~5° misalignment is removed by the grain rotating, perfectly aligning with graphene on the $Pt_{110}Gr_{zz}$. (c) Both blue and yellow grains have ~5° misalignment from the graphene. (d) The yellow grain rotates to $Pt_{100}Gr_{zz}$ epitaxy. The blue grain is 4° from $Pt_{110}Gr_{zz}$ epitaxy. (e) The grains merge with $Pt_{110}Gr_{zz}$ epitaxy. Inserts show magnified views from the edges of the indicated grains, with black/white lines indicating graphene/Pt lattice lines that are nearest to epitaxy. Scale bar is 2 nm.

Imaging the grain boundary at atomic resolution reveals the series of dislocation cores that constitute a typical grain boundary (Figure 5).[45] These small voids extend along the boundary to accommodate the rotational mismatch. While this is a Σ5 grain boundary (discussed later), the cores are not regularly distributed along the boundary length and do not exhibit consistent atomic structure (Figures 5b and c). We attribute the irregularity in their shape and distribution as due to the dynamic nature of the rotating grains, and the atomic reconfiguration that occurs through the cores to accommodate the changing grain boundary angle. This is illustrated by two sequential images in Figures 5d and e, with the corresponding annotated images in Figures 5f and g highlighting the movement of atoms through the small voids that

constitute the dislocation cores. This facilitates the rotation of the grains by allowing for the gradual restructuring of the grain boundary to a lower angle.

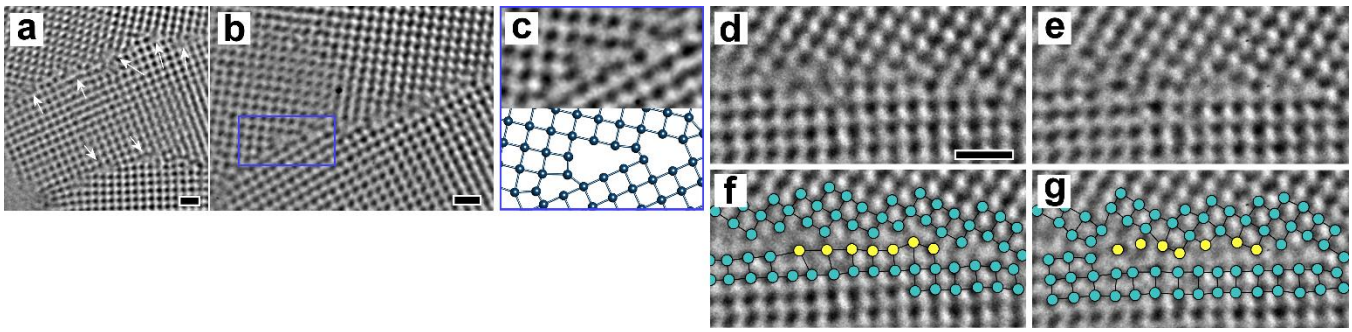


Figure 5. Atomic interface of Pt grain boundary and grain boundary growth. (a) Three Pt bilayer grains with two grain boundaries, periodically punctuated by dislocation cores. (b) Pt bilayer grains forming an atomic interface. (c) Magnified view, showing atomic structure. (d,e) Two consecutive images showing atoms along the boundary switching from one grain to the other *via* the open cores. (f,g) Atomic annotations of (d) and (e). Scale bars are 0.5 nm.

Figure 6 presents a further instance of grain rotation and merging in a Pt bilayer, with the red grain gradually rotating from $Pt_{100}Gr_{zz}$ to matching the $Pt_{110}Gr_{zz}$ epitaxy of the blue grain over the course of six minutes. The lower blue grain is anchored to a larger Pt film. The color coding of the grains is the result of a superimposed reconstruction from FFT masking of the appropriate grains reflections (see Supporting Figure S9). After a short period the larger (blue) grain splits in to two smaller grains (Figure 6b). By splitting in to two smaller grains their rotational mobility is drastically increased; the rotational mobility M is strongly dependent on the inverse of the grain size R ($M \propto {}^{1}/_{R^{p}}$ for $p = 4$ or 5).[44] While the lower grain is fixed and does not deviate significantly from $Pt_{110}Gr_{zz}$, the upper grain is now able to rapidly rotate, merging with the red grain (Figure 6e) before fully assimilating into the final complete grain (Figure 6h). The red grain gradually rotates counter clockwise, as seen in the FFTs (Figure 6i-k), to eventually coalesce with the blue grain with $Pt_{110}Gr_{zz}$ epitaxy. Examining the grain boundary (Figures 6l and m)

reveals its structural change with decrease in angle, with a single dislocation necessary to accommodate it before finally coalescing completely.

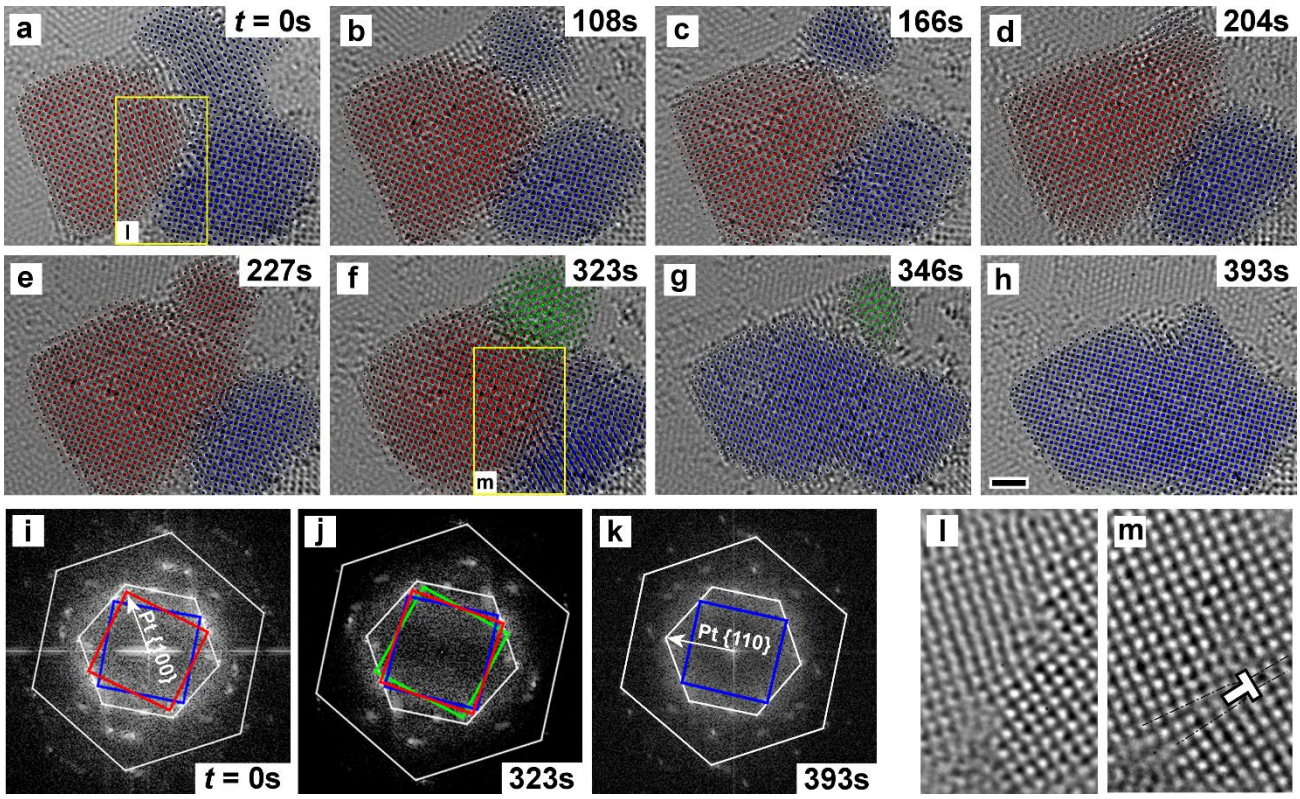


Figure 6. Epitaxial rotation and assimilation of Pt bilayer grains. (a-h) Time series of Pt bilayer grains. The coloring is the result of Fourier filtering of the grain's FFT reflections, with each color resulting from filtering a different set of reflections (see Supporting Figure S9). Scale bar is 1 nm. (i-k) Annotated FFTs from indicated timestamps, showing the change in rotation of the respectively colored grains compared to the graphene lattice (white). (l,m) Magnified views from the indicated rectangles in (a) and (f), showing the change in grain interface from a higher angle grain boundary to a single dislocation.

For our secondary grain growth observations, we have shown that the final Pt bilayer grains prefer to end in an epitaxial configuration with the graphene. This is in agreement with the secondary grain growth model for epitaxial thin films described by Thompson *et al.*,[46] which argues that annealing drives grain coarsening through the minimization of surface energies of both the thin-film and substrate. And our observations of grain rotation facilitated coalescence support the model of Moldovan *et al.*,[44] where

instead of grain coarsening we observe grains coalescing; *i.e.*, rather than a grain growing larger with its neighbors shrinking due to grain boundary migration, a grain instead coalesces with its neighbors by rotational alignment. In the rotation-coalescence model coincident site lattice (CSL) grain boundaries can act as low energy intermediates as a grain rotates toward assimilating with its neighbor.[47] Figure 7a shows a Σ5 CSL grain boundary that formed during the grain coalescence process in Figure 4, between Figure 4b and c along the upper boundary. Figure 7b indicates the CSL with annotations, with the atomic sites of the upper grain projected in to the lower, with the matching atomic sites highlighted in yellow corresponding to a Σ5 CSL grain boundary superlattice. This superlattice is shown with atomic models of the two grains overlapping in Figure 7c, with the coincident sites highlighted in Figure 7d. The blue grain in Figure 4 thus rotates through this intermediate low grain boundary energy CSL, allowing for a low energy path when switching from $Pt_{100}Gr_{zz}$ to $Pt_{110}Gr_{zz}$ epitaxy.

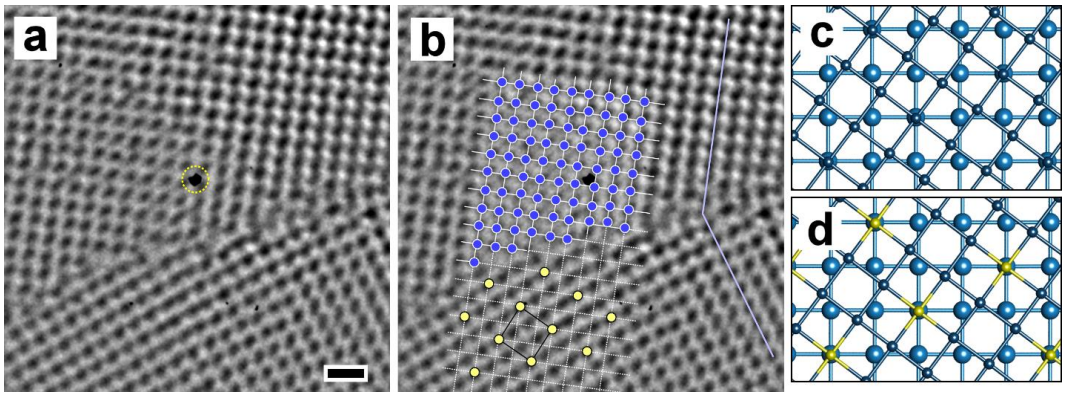


Figure 7. Pt grain boundary coincident site lattice. (a,b) Non-annotated and annotated AC-TEM image of a grain boundary. Annotated lines and blue circles indicate the lattice structure and atomic sites of the upper grain. The line annotations are extended onto the lower grain. Yellow circles indicate where these lines are coincident with an atomic site on the lower grain, revealing a Σ5 CSL superlattice. The lower grain corresponds to the blue grain in Figure 4, the upper to the cyan. (c,d) Diagrams of two simple cubic lattices stacked atop each other, with the same relative rotation as measured in the TEM images, showing the same Σ5 CSL. The coincident sites are highlighted in (d). Yellow circled area in (a) is an artifact due to dust on the camera. Scale bar is 0.5 nm.

The incomplete nature of the thin film raises the possibility of a contribution from the free atomic edges toward the grain energetics. We performed DFT calculations on $Pt_{100}Gr_{zz}$ epitaxially oriented Pt bilayers with different aspect ratios (Figure 8a). By maintaining the total number of atoms, we were able to calculate the relative energetic preferences for armchair *versus* zigzag dominant free edges (Figure 8a models X and Y, respectively). Starting with an initial original cluster of 6×6 Pt rows, we added an additional row to the zigzag/armchair faces for model X/Y, increasing the aspect ratio so that there were more armchair/zigzag arranged edge atoms. We can compare the DFT calculated total energy of the two equal atom systems X and Y to evaluate the edge preference, with the higher energy configuration having a less favorable edge configuration. Comparison of the energies of the higher aspect ratios shows that the armchair edge is more favorable. This was supported by measuring the free edges in our AC-TEM imaged Pt atomic layers (Figures 8b and c), categorizing the edges as either being parallel to the zigzag or armchair of the underlying graphene.

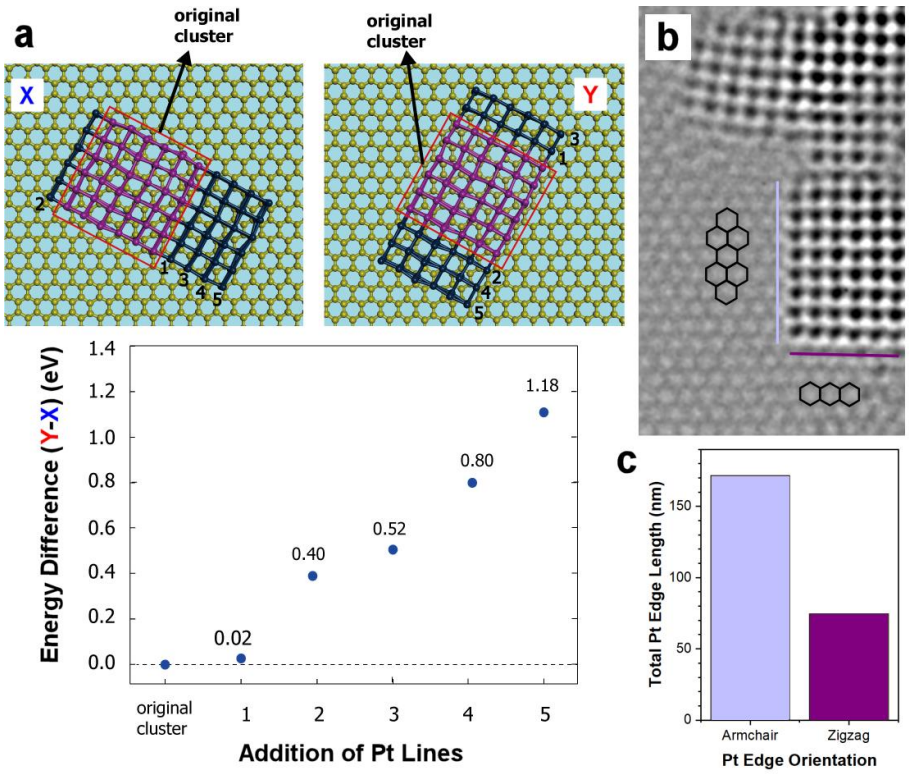


Figure 8. Relative energetics of free Pt edges on graphene. (a) DFT calculated relative energies of $Pt_{100}Gr_{zz}$ oriented Pt bilayers on graphene. Armchair edge sites (configuration X) are energetically preferred to zigzag sites (configuration Y). The Pt structures in red squares show the initial structure and the green atoms shows the attached Pt lines. The numbers in atomic models in (a) indicate the order of the attached Pt lines and correspond to the numbers in abscissa. The order of attachment is determined by the lower DFT total energy. (b) Illustrative AC-TEM image of free edges of a $Pt_{100}Gr_{zz}$ grain. (c) Bar chart of the relative prevalence of the different Pt edge orientations.

The preference for armchair edges was observed to influence their dynamics, with restructuring of the edges occurring to minimize free zigzag edges. This edge reordering was sufficient to induce dislocation formation, as shown in Figure 9. A predominantly armchair edged $Pt_{100}Gr_{zz}$ oriented grain exhibited a small perturbation and step (Figure 9a), which left a significant zigzag-matched edge. The extruded part of the Pt layer can be seen to pucker slightly in Figure 9b, which is more clearly evidenced by an increase in the strain measured by geometric phase analysis (GPA) by comparison between Figure 9e and f. Eventually several atoms are emitted from the corner of the extrusion (Figure 9c), followed by the

restructuring of the layer around it and thus forming a dislocation (Figure 9d). Examination of the GPA reveals how the dislocation core strain field interacts with the edge (Figure 9h), showing distinct strain to that observed for a dislocation in the bulk Pt bilayer (Supporting Figure S10).

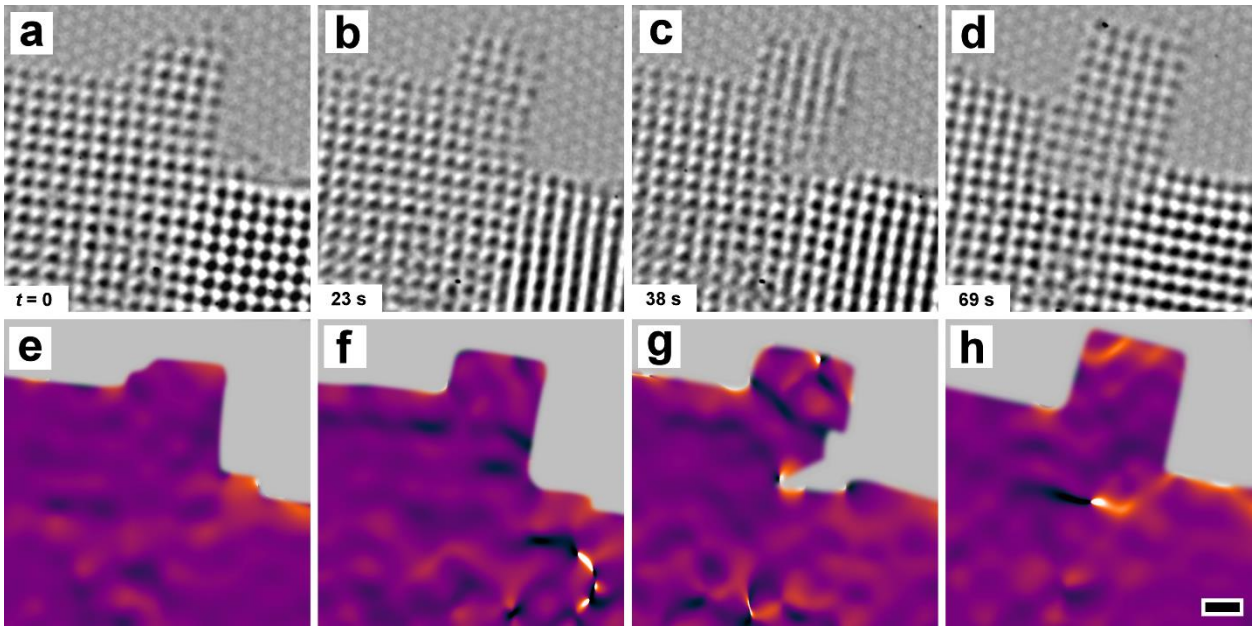


Figure 9. Edge-mediated dislocation formation in a Pt atomic bilayer. (a-d) AC-TEM images of a dislocation forming from the edge of the Pt. The lower part of the Pt maintains epitaxy with the graphene along $Pt_{100}Gr_{zz}$. (e-h) Geometric phase analysis (ε_{yy} component) of the respective TEM images, showing increased strain in the top region in (f) and (g) up to the formation of the dislocation, redistributing the strain to about the dislocation core. Scale bar is 0.5 nm for all images.

Conclusion

We have performed a detailed investigation of the atomic structure and dynamics of heteroepitaxial platinum atomic layers on a graphene monolayer. The platinum bilayers exhibited two epitaxial orientation with respect to the graphene substrate, both of which were found to have similar energetic stability. These two low-energy epitaxies, alongside low-energy CSL grain boundaries, acted as intermediate stepping-stones in the secondary grain growth by grain rotation and coalescence. This mechanism of secondary grain growth is distinct from the common method of boundary curvature induced

grain boundary migration, and leads solely to grain growth rather than grain coarsening. We hope that our experimentally derived understanding of platinum-graphene epitaxy and platinum grain growth will help inform the deposition of uniform large area platinum atomic layers on graphene substrates for catalysis applications.

Methods

Platinum on graphene preparation. Complete details of the method are presented in references [33] and [34]. For surface limited redox reaction (SLRR) synthesis, Cu underpotential deposition was performed by holding the potential at 100 mV for 10min before galvanic replacement with Pt. An Ar-saturated hydrochloric acid solution (10 mM $CuSO_4$ + 50 mM $HClO_4$) was used as an alternative to sulfuric acid, due to a tendency for sulfuric acid to damage the silicon nitride based grids. A Thermo Nicolet Almega XR Dispersive Raman Spectrometer was used to verify successful transfers through the indication of a sharp, characteristic 2D feature at 2700 cm^{-1}.

TEM Imaging. Graphene used in AC-TEM experiments was synthesized on a copper substrate with tungsten support using the CVD method reported by Fan *et al*.[48] The graphene/copper/tungsten system was spin-coated with PMMA and subsequently anodically etched using 1.5 M NaOH. The etching was followed by dissolution of the substrate in 0.2 M $(NH_4)_2S_2O_8$. The resulting graphene/PMMA film was transferred to 18.2 MΩ deionized water three times for approximately one hour each. The graphene/PMMA film was then transferred to an Agar Scientific silicon nitride TEM grid supported on a silicon chip. The silicon chip and sample coated TEM grid were then placed onto a hot plate at 40 °C for 3 hours, followed by a 30 min heating step up to 150 °C. PMMA was removed by annealing the sample in a furnace at 350 °C overnight. TEM imaging was performed on an aberration corrected JEOL 2200MCO at an accelerating voltage of 80 kV. Images presented in the text have been subjected to nearest-neighbor smoothing to reduce noise. The electron beam flux incident on the sample was measured as approximately 10^5 e^- nm^{-2} s^{-1}.

DFT Modeling. We performed DFT calculations within the generalized gradient approximation of Perdew-Burke-Ernzerhof (PBE) functional using Vienna *ab initio* simulation package (VASP) code.[49,50] Vanderbilt pseudopotentials are also used in this calculation.[51] The unit cell contains graphene layer of 392 C atoms and Pt

cluster of 72 Pt atoms. In the unit cell, the vacuum region of 30 Å is contained in z direction. The basis set contains plane waves up to an energy cutoff of 400 eV. The Brillouin zone was sampled using only Γ point. When structural relaxations are performed, the structure is relaxed under the constraint until the force on each atom is smaller than 0.02 eV/Å. The DFT-D3 method of Grimme was used to describe the weak dispersion forces from the Van der Waals interaction between graphene and Pt layers.[52] To consider the magnetic effect, we performed the spin polarized calculation for some structures and it does not affect the difference of energy due to the non-spin polarization. In the calculation of the optimized distance between the graphene and Pt layers (Fig. 3a), we performed the DFT calculation depending on various distances since it could not get automatically just by structural relaxation. To obtain the structure and the energy depending on the rotation angle of Pt layers (Fig. 3b), we also performed DFT calculation for the structures of various position keeping the same rotation angle and obtained the structure of the lowest energy at the rotation angle.

Acknowledgements

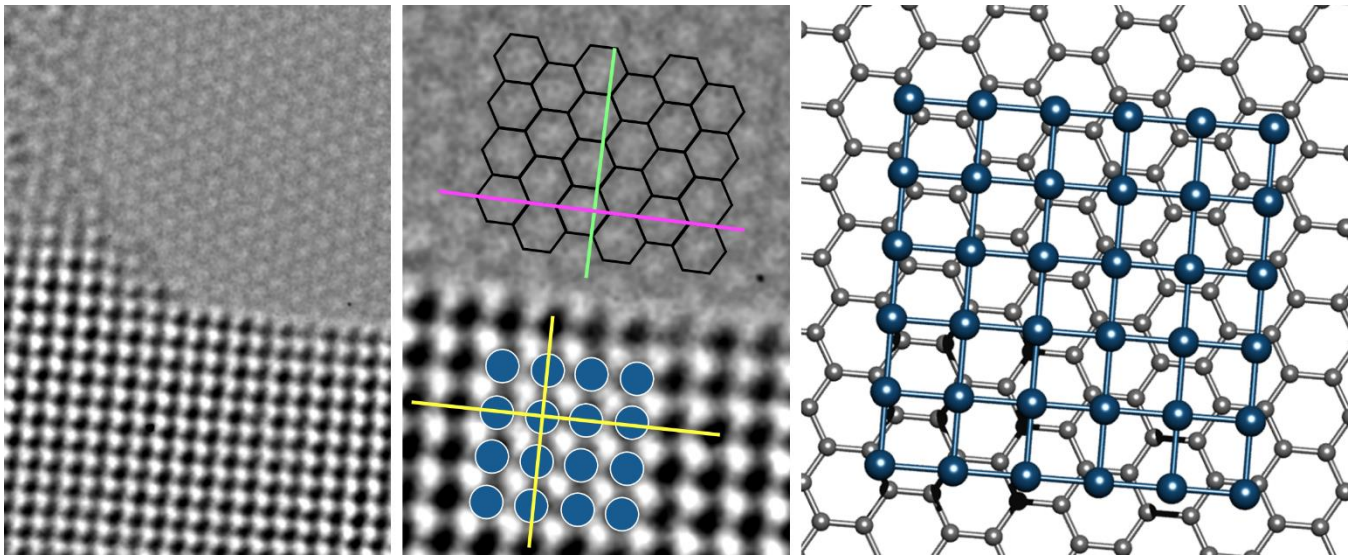
A.W.R. thanks the support of the Royal Society. G.-D.L. acknowledges support from the Supercomputing Center/Korea Institute of Science and Technology Information with supercomputing resources (KSC-2018-CRE-0045) and from the National Research Foundation of Korea (NRF) grant funded by the Korea government (RIAM 2016R1D1A1A02937045, 2019R1A2C2005098 and 2017M3D1A1040688). F.M.A. thanks the financial support of two U. S. National Science Foundation programs, namely the Office of International Science & Engineering (OISE) program (grant award # 1103827) and the Nanostructured Materials for Energy Storage and Conversion (NESAC) IGERT program (grant award # 1069138).

Supporting Information

The Supporting Information is available free of charge on the ACS Publications website at DOI: xxx

Further data confirming the mono- to bilayer nature of the platinum film, multi-slice image simulations, DFT optimized structures and electron densities, and image processing details.

ToC Graphic



Reference

(1) Kettler, P. B. Platinum Group Metals in Catalysis: Fabrication of Catalysts and Catalyst Precursors. *Org. Process Res. Dev.* **2003**, *7*, 342–354.

(2) Choi, D. S.; Robertson, A. W.; Warner, J. H.; Kim, S. O.; Kim, H. Low-Temperature Chemical Vapor Deposition Synthesis of Pt-Co Alloyed Nanoparticles with Enhanced Oxygen Reduction Reaction Catalysis. *Adv. Mater.* **2016**, *28*, 7115–7122.

(3) Antolini, E.; Salgado, J. R. C.; Gonzalez, E. R. The Stability of Pt–M (M=first Row Transition Metal) Alloy Catalysts and Its Effect on the Activity in Low Temperature Fuel Cells. *J. Power Sources* **2006**, *160*, 957–968.

(4) Wu, J.; Yuan, X. Z.; Martin, J. J.; Wang, H.; Zhang, J.; Shen, J.; Wu, S.; Merida, W. A Review of PEM Fuel Cell Durability: Degradation Mechanisms and Mitigation Strategies. *J. Power Sources* **2008**, *184*, 104–119.

(5) Zhang, S.; Yuan, X.-Z.; Hin, J. N. C.; Wang, H.; Friedrich, K. A.; Schulze, M. A Review of Platinum-Based Catalyst Layer Degradation in Proton Exchange Membrane Fuel Cells. *J. Power Sources* **2009**, *194*, 588–600.

(6) Sheng, W.; Gasteiger, H. a.; Shao-Horn, Y. Hydrogen Oxidation and Evolution Reaction Kinetics on Platinum: Acid vs Alkaline Electrolytes. *J. Electrochem. Soc.* **2010**, *157*, B1529.

(7) Dai, P.; Xie, J.; Mayer, M. T.; Yang, X.; Zhan, J.; Wang, D. Solar Hydrogen Generation by Silicon Nanowires Modified with Platinum Nanoparticle Catalysts by Atomic Layer Deposition. *Angew. Chemie - Int. Ed.* **2013**, *52*, 11119–11123.

(8) Dai, L. Functionalization of Graphene for Efficient Energy Conversion and Storage. *Acc. Chem. Res.* **2013**, *46*, 31–42.

(9) Zhou, X.; Qiao, J.; Yang, L.; Zhang, J. A Review of Graphene-Based Nanostructural Materials for Both Catalyst Supports and Metal-Free Catalysts in PEM Fuel Cell Oxygen Reduction Reactions. *Adv. Energy Mater.* **2014**, *4*, 1301523.

(10) Li, H.; Tsai, C.; Koh, A. L.; Cai, L.; Contryman, A. W.; Fragapane, A. H.; Zhao, J.; Han, H. S.; Manoharan, H. C.; Abild-Pedersen, F. Nørskov, J. K.; Zheng, X. Activating and Optimizing MoS2 Basal Planes for Hydrogen Evolution through the Formation of Strained Sulphur Vacancies. *Nat. Mater.* **2016**, *15*, 48–53 .

(11) Liu, G.; Robertson, A. W.; Li, M. M.-J.; Kuo, W. C. H.; Darby, M. T.; Muhieddine, M. H.; Lin, Y.-C.; Suenaga, K.; Stamatakis, M.; Warner, J. H.; Tsang, S. C. E. MoS_2 Monolayer Catalyst Doped with Isolated Co Atoms for the Hydrodeoxygenation Reaction. *Nat. Chem.* **2017**, *9*, 810–816.

(12) Laursen, A. B.; Patraju, K. R.; Whitaker, M. J.; Retuerto, M.; Sarkar, T.; Yao, N.; Ramanujachary, K. V.; Greenblatt, M.; Dismukes, G. C. Nanocrystalline Ni_5P_4: A Hydrogen Evolution Electrocatalyst of Exceptional Efficiency in Both Alkaline and Acidic Media. *Energy Environ. Sci.* **2015**, *8*, 1027–1034.

(13) Wang, X.; Kolen'Ko, Y. V.; Bao, X. Q.; Kovnir, K.; Liu, L. One-Step Synthesis of Self-Supported Nickel Phosphide Nanosheet Array Cathodes for Efficient Electrocatalytic Hydrogen Generation. *Angew. Chemie - Int. Ed.* **2015**, *54*, 8188–8192.

(14) Wen, Z.; Liu, J.; Li, J. Core/Shell Pt/C Nanoparticles Embedded in Mesoporous Carbon as a Methanol-Tolerant Cathode Catalyst in Direct Methanol Fuel Cells. *Adv. Mater.* **2008**, *20*, 743–747.

(15) Yin, X.; Shi, M.; Wu, J.; Pan, Y.-T.; Gray, D. L.; Bertke, J. A.; Yang, H. Quantitative Analysis of Different Formation Modes of Platinum Nanocrystals Controlled by Ligand Chemistry. *Nano Lett.* **2017**, *17*, 6146–6150.

(16) Hong, J. W.; Kang, S. W.; Choi, B.-S.; Kim, D.; Lee, S. B.; Han, S. W. Controlled Synthesis of Pd–Pt Alloy Hollow Nanostructures with Enhanced Catalytic Activities for Oxygen Reduction. *ACS Nano* **2012**, *6*, 2410–2419.

(17) Yoo, E.; Okata, T.; Akita, T.; Kohyama, M.; Nakamura, J.; Honma, I. Enhanced Electrocatalytic Activity of Pt Subnanoclusters on Graphene Nanosheet Surface. *Nano Lett.* **2009**, *9*, 2255–2259.

(18) Jones, J.; Xiong, H.; DeLaRiva, A. T.; Peterson, E. J.; Pham, H.; Challa, S. R.; Qi, G.; Oh, S.; Wiebenga, M. H.; Pereira Hernandez, X. I.; Wang, Y.; Datye, A. K.. Thermally Stable Single-Atom Platinum-on-Ceria Catalysts *via* Atom Trapping. *Science.* **2016**, *353*, 150–154.

(19) Gong, K.; Su, D.; Adzic, R. R. Platinum-Monolayer Shell on AuNi(0.5)Fe Nanoparticle Core Electrocatalyst with High Activity and Stability for the Oxygen Reduction Reaction. *J. Am. Chem. Soc.* **2010**, *132*, 14364–14366.

(20) Dvořák, F.; Farnesi Camellone, M.; Tovt, A.; Tran, N.; Negreiros, F. R.; Vorokhta, M.; Skála, T.; Matolínová, I.; Mysliveček, J.; Matolín, V.; Fabris, S.. Creating Single-Atom Pt-Ceria Catalysts by Surface Step Decoration. *Nat. Commun.* **2016**, *7*, 10801.

(21) Ambrozik, S.; Dimitrov, N. The Deposition of Pt *via* Electroless Surface Limited Redox Replacement. *Electrochim. Acta* **2015**, *169*, 248–255.

(22) Zhang, J.; Lima, F. H. B.; Shao, M. H.; Sasaki, K.; Wang, J. X.; Hanson, J.; Adzic, R. R. Platinum Monolayer on Nonnoble Metal-Noble Metal Core-Shell Nanoparticle Electrocatalysts for O_2 Reduction. *J. Phys. Chem. B* **2005**, *109*, 22701–22704.

(23) Cherevko, S.; Keeley, G. P.; Kulyk, N.; Mayrhofer, K. J. J. Pt Sub-Monolayer on Au: System Stability and Insights into Platinum Electrochemical Dissolution. *J. Electrochem. Soc.* **2016**, *163*, H228–H233.

(24) Sasaki, K.; Naohara, H.; Cai, Y.; Choi, Y. M.; Liu, P.; Vukmirovic, M. B.; Wang, J. X.; Adzic, R. R. Core-Protected Platinum Monolayer Shell High-Stability Electrocatalysts for Fuel-Cell Cathodes. *Angew. Chemie* **2010**, *49*, 8602–8607.

(25) Kim, H.; Robertson, A. W.; Kim, S. O.; Kim, J. M.; Warner, J. H. Resilient High Catalytic Performance of Platinum Nanocatalysts with Porous Graphene Envelope. *ACS Nano* **2015**, *9*, 5947–5957.

(26) Wettergren, K.; Schweinberger, F. F.; Deiana, D.; Ridge, C. J.; Crampton, A. S.; Rötzer, M. D.; Hansen, T. W.; Zhdanov, V. P.; Heiz, U.; Langhammer, C. High Sintering Resistance of Size-Selected Platinum Cluster Catalysts by Suppressed Ostwald Ripening. *Nano Lett.* **2014**, *14*, 5803-5809.

(27) Hansen, T. W.; Delariva, A. T.; Challa, S. R.; Datye, A. K. Sintering of Catalytic Nanoparticles: Particle Migration or Ostwald Ripening? *Acc. Chem. Res.* **2013**, *46*, 1720–1730.

(28) Brankovic, S. R.; Wang, J. X.; Adžić, R. R. Metal Monolayer Deposition by Replacement of Metal Adlayers on Electrode Surfaces. *Surf. Sci.* **2001**, *474*, L173–L179.

(29) Zhang, J.; Mo, Y.; Vukmirovic, M. B.; Klie, R.; Sasaki, K.; Adzic, R. R. Platinum Monolayer Electrocatalysts for O 2 Reduction: Pt Monolayer on Pd(111) and on Carbon-Supported Pd Nanoparticles. *J. Phys. Chem. B* **2004**, *108*, 10955–10964.

(30) Li, M.; Ma, Q.; Zi, W.; Liu, X.; Zhu, X.; Liu, S.. Pt Monolayer Coating on Complex Network Substrate with High Catalytic Activity for the Hydrogen Evolution Reaction. *Sci. Adv.* **2015**, *1*, e1400268.

(31) Kye, J.; Shin, M.; Lim, B.; Jang, J. W.; Oh, I.; Hwang, S. Platinum Monolayer Electrocatalyst on Gold Nanostructures on Silicon for Photoelectrochemical Hydrogen Evolution. *ACS Nano* **2013**, *7*, 6017–6023.

(32) Esposito, D. V.; Chen, J. G. Monolayer Platinum Supported on Tungsten Carbides as Low-Cost Electrocatalysts: Opportunities and Limitations. *Energy Environ. Sci.* **2011**, *4*, 3900–3912.

(33) Abdelhafiz, A.; Vitale, A.; Joiner, C.; Vogel, E.; Alamgir, F. M. Layer-by-Layer Evolution of

Structure, Strain, and Activity for the Oxygen Evolution Reaction in Graphene-Templated Pt Monolayers. *ACS Appl. Mater. Interfaces* **2015**, *7*, 6180–6188.

(34) Abdelhafiz, A.; Vitale, A.; Buntin, P.; DeGlee, B.; Joiner, C.; Robertson, A.; Vogel, E. M.; Warner, J.; Alamgir, F. M. Epitaxial and Atomically Thin Graphene–Metal Hybrid Catalyst Films: The Dual Role of Graphene as the Support and the Chemically-Transparent Protective Cap. *Energy Environ. Sci.* **2018**, *11*, 1610–1616.

(35) Sutter, P.; Sadowski, J. T.; Sutter, E. Graphene on Pt(111): Growth and Substrate Interaction. *Phys. Rev. B* **2009**, *80*, 245411.

(36) Chen, Q.; He, K.; Robertson, A. W.; Kirkland, A. I.; Warner, J. H. Atomic Structure and Dynamics of Epitaxial 2D Crystalline Gold on Graphene at Elevated Temperatures. *ACS Nano* **2016**, *10*, 10418–10427.

(37) Sasaki, Y.; Kitaura, R.; Yamamoto, Y.; Arai, S.; Suzuki, S.; Miyata, Y.; Shinohara, H. Preparation and Observation of an Atomic Layer of Gold Formed on the Surface of Graphene. *Appl. Phys. Express* **2012**, *5*, 065103.

(38) Zhao, J.; Deng, Q.; Bachmatiuk, A.; Sandeep, G.; Popov, A.; Eckert, J.; Rummeli, M. H. Free-Standing Single-Atom-Thick Iron Membranes Suspended in Graphene Pores. *Science.* **2014**, *343*, 1228–1232.

(39) Hong, H. K.; Jo, J.; Hwang, D.; Lee, J.; Yeon, N.; Son, S.; Kim, J. H.; Jin, M. J.; Jun, Y. C.; Erni, R.; Kwak, S. K; Yoo, J. W.; Lee, Z. Atomic Scale Study on Growth and Heteroepitaxy of ZnO Monolayer on Graphene. *Nano Lett.* **2017**, *17*, 120–127.

(40) Anderson, M. .; Srolovitz, D. .; Grest, G. .; Sahni, P. . Computer Simulation of Grain Growth—I. Kinetics. *Acta Metall.* **1984**, *32*, 783–791.

(41) Mullins, W. W. Two-Dimensional Motion of Idealized Grain Boundaries. *J. Appl. Phys.* **1956**, *27*, 900–904.

(42) Mahata, A.; Garg, P.; Rawat, K. S.; Bhauriyal, P.; Pathak, B. A Free-Standing Platinum Monolayer as an Efficient and Selective Catalyst for the Oxygen Reduction Reaction. *J. Mater. Chem. A* **2017**, *5*, 5303–5313.

(43) Hillert, M. On the Theory of Normal and Abnormal Grain Growth. *Acta Metall.* **1965**, *13*, 227–238.

(44) Moldovan, D.; Yamakov, V.; Wolf, D.; Phillpot, S. Scaling Behavior of Grain-Rotation-Induced Grain Growth. *Phys. Rev. Lett.* **2002**, *89*, 206101.

(45) Merkle, K. L. Atomic Structure of Grain Boundaries. *J. Phys. Chem. Solids* **1994**, *55*, 991–1005.

(46) Thompson, C. V. Grain Growth in Thin Films. *Annu. Rev. Mater. Sci.* **1990**, *20*, 245–268.

(47) Harris, K. E.; Singh, V. V.; King, A. H. Grain Rotation in Thin Films of Gold. *Acta Mater.* **1998**, *46*, 2623–2633.

(48) Fan, Y.; He, K.; Tan, H.; Speller, S.; Warner, J. H. Crack-Free Growth and Transfer of Continuous Monolayer Graphene Grown on Melted Copper. *Chem. Mater.* **2014**, *26*, 4984–4991.

(49) Perdew, J. P.; Burke, K.; Ernzerhof, M. Generalized Gradient Approximation Made Simple. *Phys. Rev. Lett.* **1996**, *77*, 3865–3868.

(50) Kresse, G. Efficient Iterative Schemes for *Ab Initio* Total-Energy Calculations Using a Plane-Wave Basis Set. *Phys. Rev. B* **1996**, *54*, 11169–11186.

(51) Vanderbilt, D. Soft Self-Consistent Pseudopotentials in a Generalized Eigenvalue Formalism. *Phys. Rev. B* **1990**, *41*, 7892–7895.

(52) Grimme, S.; Antony, J.; Ehrlich, S.; Krieg, H. A Consistent and Accurate *Ab Initio* Parametrization of Density Functional Dispersion Correction (DFT-D) for the 94 Elements H-Pu. *J. Chem. Phys.* **2010**, *132*, 154104.